Stimulated Brillouin scattering microscopy with a high-peak-power 780-nm pulsed laser system

Yun Qi [1,2], Shuai Yao [1,2], Zi-Xuan Du[1,2], Jin-Rui Zhang[1], Cuiyun Zhou[1], Xiaohu Fu[1], Huan Li[3], Ting Mi[3], Yu-Han Chen[4], Yu-Fan Wang [4], Yun Luo[4], Xuyan He[5], Jing Nan[6], Yanjie Zhang [7], Lin Sun[6], Peng Xia[5], Shi-Qing Cai[4], Jiu-Lin Du [4], Jingjing Xie [3], Wei-Biao Chen [1]✉ & Fan Yang [1,2]✉

Stimulated Brillouin scattering microscopy enables all-optical, non-contact, high-spatial-resolution mechanical imaging with high specificity. Recent advances in quasi-continuous-wave stimulated Brillouin scattering have substantially reduced the required laser power. However, the pixel dwell time remains limited to 20 ms, and further reductions without compromising resolution, precision or specificity are challenging. Here we address this limitation by developing a frequency-doubled pulsed fibre laser system operating at 780 nm, delivering a peak power of 267 W. To mitigate the high-intensity noise intrinsic to amplified fibre lasers, we implement a high-performance noise cancellation system based on auto-balanced detection. As a result, we achieve a pixel dwell time as short as 200 μs for full spectral acquisition, which is two orders of magnitude faster than previous stimulated Brillouin scattering implementations, and maintain an average power of 30 mW. We demonstrate high-speed, high-specificity and high-sensitivity Brillouin imaging of live single cells, organoids, zebrafish larvae and ovarian follicles with subcellular details. Furthermore, we capture the in vivo biomechanical dynamics of rapid cell divisions during the early embryo development of *Caenorhabditis elegans* in a living worm.

Mechanical properties play important roles in biomedical research as they directly influence the behaviour and function of cells and tissues[1–3]. However, current techniques for assessing the viscoelastic properties are often limited to surface measurements or lack sufficient three-dimensional subcellular resolution[4,5]. For example, atomic force microscopy, considered to be the gold standard in mechanobiology, measures the quasi-static Young's modulus and provides high spatial resolution and sensitivity for nanoscale measurements[4]. Despite these advantages, atomic force microscopy is restricted to surface measurements and requires direct sample contact, which can be invasive and potentially alter the mechanical properties of the sample. Optical coherence elastography, on the other hand, offers non-invasive, depth-resolved mechanical imaging, yet it struggles to achieve subcellular resolution, limiting its ability to measure individual cells or capture fine mechanical details within tissues[5].

[1]Shanghai Institute of Optics and Fine Mechanics, Chinese Academy of Sciences, Shanghai, China. [2]University of Chinese Academy of Sciences, Beijing, China. [3]School of Physical Science and Technology & State Key Laboratory of Advanced Medical Materials and Devices, ShanghaiTech University, Shanghai, China. [4]Institute of Neuroscience, State Key Laboratory of Neuroscience, Center for Excellence in Brain Science and Intelligence Technology, Chinese Academy of Sciences, Shanghai, China. [5]Zhejiang Provincial Key Laboratory for Cancer Molecular Cell Biology, Life Sciences Institute, Zhejiang University, Hangzhou, China. [6]Shanghai Medsyin Biopharma, Shanghai, China. [7]Oncology Department, Shanghai Ninth People's Hospital, Shanghai Jiao Tong University School of Medicine, Shanghai, China. ✉e-mail: wbchen@siom.ac.cn; yang@siom.ac.cn
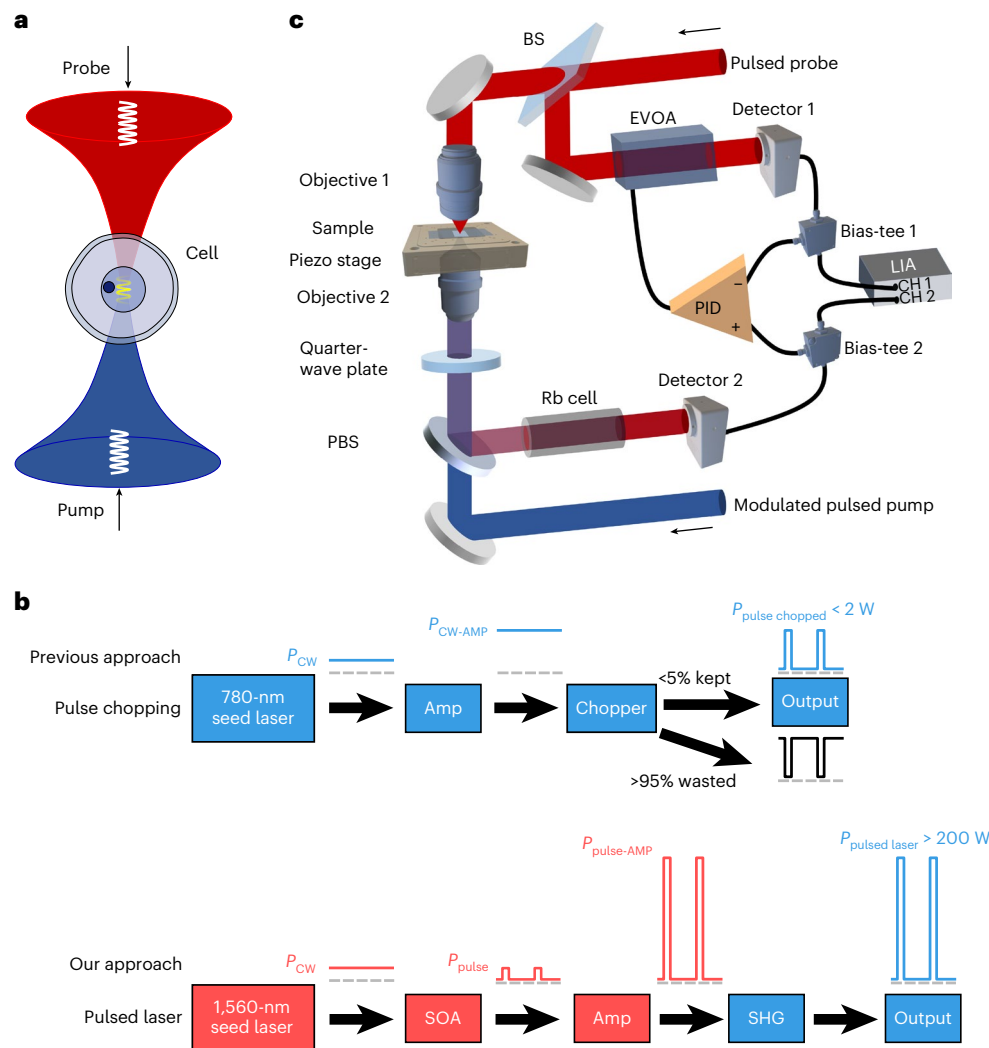
Fig. 1 | Schematic of the pulsed laser system and PL-SBS microscope.
a, Counterpropagating pump and probe beams are focused at the same position within the sample. **b**, Schematic of the pulse generation approaches, comparing the previous quasi-continuous wave (QCW) approach with the current pulsed laser approach. In the QCW method, a CW 780-nm seed laser is amplified (for example, via a tapered amplifier) and then chopped by an optical modulator (for example, an AOM). In the pulsed laser system, a CW 1,560-nm seed laser is passed through a pulse generator (for example, an SOA for generating seed pulses with 2–20-ns pulse width), followed by pulsed amplification and SHG to produce high-peak-power pulses at 780 nm. Amp, amplifier. **c**, Schematic of

the PL-SBS microscope setup. The pulsed probe beam is split by a beamsplitter (BS) into two arms: one arm is focused onto the sample by an objective, whereas the other passes through an electronic variable optical attenuator (EVOA) as a reference for auto-balanced detection. The modulated pulsed pump is focused on the same position as the probe beam using a second objective. After interaction with the pump, the probe beam is reflected by a PBS and filtered by a rubidium gas cell. The d.c. components from the sample and reference arms are fed into a proportional–integral–derivative (PID) regulator for feedback control of the balance condition, whereas the a.c. components are put into the two channels of an LIA for differential detection.

Brillouin microscopy has recently emerged as a promising technique for all-optical, non-invasive mechanical measurements of cells and tissues with near-diffraction-limited resolution[6–19]. The Brillouin scattering signal measures the longitudinal modulus in the gigahertz frequency range and follows a Lorentzian distribution, where the peak frequency shift correlates with the material's longitudinal elastic modulus and the linewidth correlates with its longitudinal viscosity[12]. However, spontaneous Brillouin scattering has a very small scattering cross-section, with less than 10^{-10} of the excitation photons producing Brillouin-scattered light, which necessitates a long integration time for imaging. For example, confocal spontaneous Brillouin microscopy requires pixel dwell times ranging from tens to hundreds of milliseconds[19–23]. Advancements in line-scanning spontaneous Brillouin microscopy have reduced the effective pixel dwell time to 1 ms by multiplexing one sample axis onto the camera[24,25]. More recently, full-field multiplexing combined with a Fourier transform

spectrometer has enabled two-axis multiplexing, achieving effective pixel times as short as 24 μs in water and 203 μs in a biological sample[26]. However, this technique is limited by a frequency-shift precision of 83 MHz and a linewidth precision of 240 MHz (ref. 26). Moreover, spontaneous Brillouin microscopy typically achieves a shift precision of less than 10 MHz and a spectral resolution of approximately 500 MHz (refs. 15,21,24). This resolution is limited by factors such as virtual imaged phased array dispersion broadening and the objective's numerical aperture (NA) broadening, which together constrains its mechanical specificity.

Recently, stimulated Brillouin scattering (SBS) has been explored for biomechanical imaging, offering higher spatial and spectral resolutions[27–29], which are crucial for high mechanical specificity and allows distinguishing components of different mechanical responses within the diffraction-limited focal volumes of heterogeneous living biosamples. A seminal work using CW-SBS microscopy
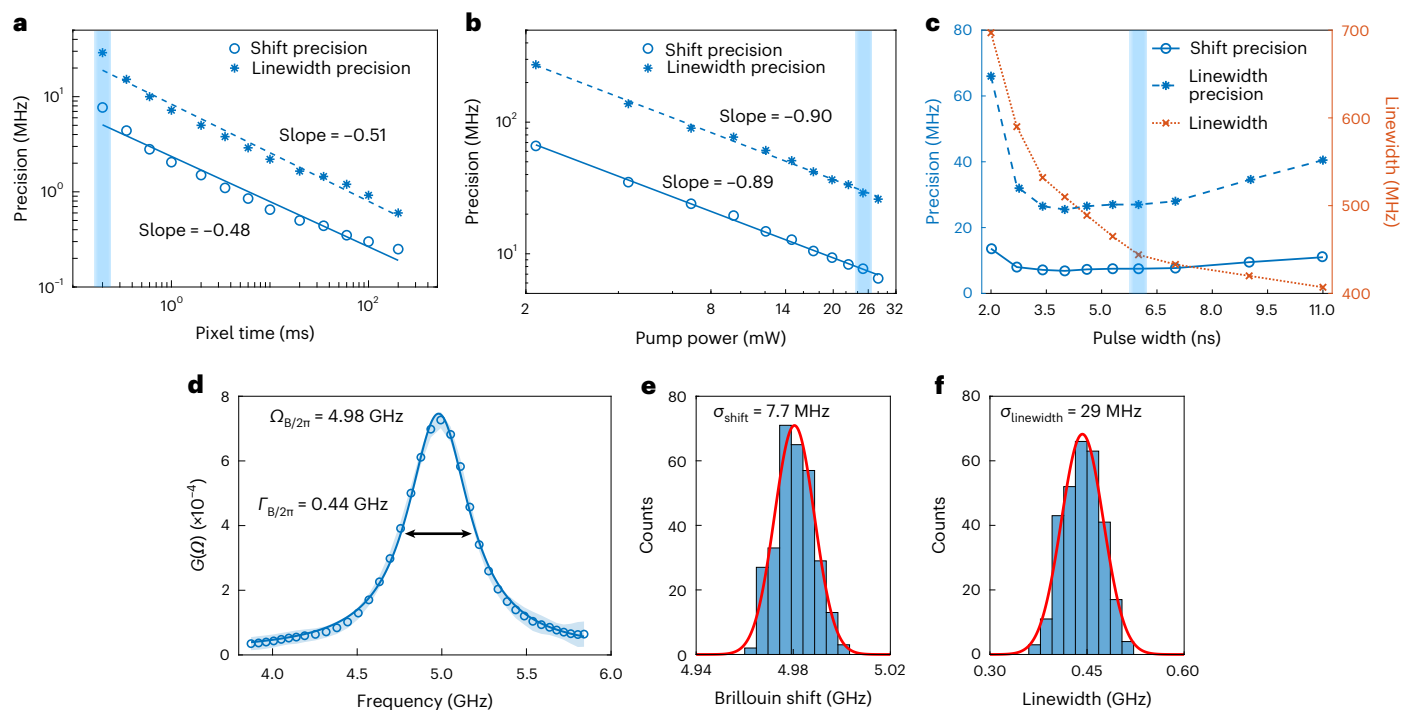
Fig. 2 | Performance characterization of PL-SBS microscope. a, Brillouin shift and linewidth precision as a function of pixel time, during which a full SBS spectrum of water spanning 2 GHz is measured. The average optical power on the sample is 30 mW in total, with 25 mW for pump and 5 mW for probe. The pulse width and rate are 6 ns and 500 kHz, respectively. The precision is determined as the standard deviation of the Brillouin shift and linewidth extracted from the Lorentzian fitting of $n = 300$ consecutively acquired SBS spectra. **b,** Brillouin shift and linewidth precision as a function of pump power on the water sample with a constant probe power of 5 mW. The pixel time is fixed at 200 μs, with 40-kHz NEP bandwidth (3.1-μs time constant) of the LIA. **c,** Brillouin shift and

linewidth precision as well as the measured linewidth of water versus pulse width. The 6-ns pulse width is generally the optimal choice in consideration of both spectral precision and resolution. The blue-shaded areas in **a**–**c** represent the parameters used in this study. **d,** SBS spectra of water measured with a pixel time of 200 μs and total power of 30 mW. The circles, blue-patch thickness and solid lines represent the mean, standard deviation and averaged Lorentzian fitting of $n = 300$ SBS spectra, respectively. **e,f,** Histograms of the Lorentzian-fitted Brillouin shift (**e**) and linewidth (**f**) from the SBS spectra in **d**, with the red curves representing Gaussian fitting.

for biomechanical imaging achieved subcellular resolution and high spectral resolution with shot-noise-limited sensitivity[29]. Furthermore, instead of two-parameter imaging contrast (Brillouin shift and linewidth) in spontaneous Brillouin microscopy, SBS microscopy offers three-parameter contrast, including Brillouin shift, linewidth and gain. Despite these advantages, CW-SBS microscopy requires a total optical power of over 168 mW (refs. 29,30), which is challenging for the imaging of fragile biological samples. To further reduce phototoxicity, quasi-CW-SBS (QCW-SBS) microscopes using the pulse-chopping technique decreased the total power to 27–55 mW, allowing the imaging of sensitive biological samples[31,32]. However, the pixel integration time remains at 20 ms, requiring over 1.3 h to capture a 500×500-pixel² two-dimensional (2D) image. Further reduction in integration time is limited by the peak power of the laser source available for SBS miscroscopy[19,33].

In this work, we address the limitation by developing a high-peak-power, low-duty-cycle pulsed fibre laser source at 780 nm with a peak power of 267 W, 100-fold higher than that in previous SBS systems[31–34]. Moreover, we developed a specialized auto-balanced detection system to suppress the intensity noise associated with the pulsed laser source, achieving noise reduction of over 31 dB. Note that nanosecond pulsed laser at 780 nm with a peak power of 12 W has been demonstrated for the manipulation of rubidium atoms[35] and auto-balanced detection technique is often required to decrease the high-intensity noise of a fibre laser system[36,37]. Our laser system enables the Brillouin imaging of live biological specimens with pixel dwell times down to 200 μs for full spectrum acquisition and maintain an average power of 30 mW. We demonstrate high speed, spatial

resolution ($0.49 \times 0.49 \times 2.1$ μm³) and shift precision (7.7 MHz) through the imaging of single cells, organoids, zebrafish larvae and ovarian follicles with high image quality and subcellular details. The observations of double Brillouin peaks, corresponding to two constituents in the heterogeneous extracellular matrix and central canal of zebrafish larvae, underscore the high spectral resolution (132 MHz) and mechanical specificity of our pulsed laser SBS (PL-SBS) microscope. Moreover, it captures the in vivo biomechanical dynamics accompanying rapid cell divisions in the early embryo development of *Caenorhabditis elegans* in a living worm, highlighting the system's high temporal resolution and sensitivity.

We also explored Brillouin gain microscopy (BGM) with our pulsed laser system, inspired by the recent continuous-wave (CW) BGM that operates without frequency scanning[38]. Leveraging the high-peak-power laser pulses and auto-balanced detection, we achieved a 5-μs pixel dwell time in phantom imaging with only 30 mW of average power, resulting in a 150-fold reduction in excitation energy compared with the CW-BGM[38].

Results

Pulsed laser system and auto-balanced detection

The SBS microscope uses two counterpropagating beams (pump and probe) that generate an interference fringe pattern (Fig. 1a). When the frequency difference between these two beams matches the material's Brillouin shift, acoustic phonons are coherently amplified. The excited phonons scatter the pump beam into the probe beam, resulting in an amplification process (stimulated Brillouin gain (SBG)) for the probe. As a nonlinear process, the SBS signal is proportional to the product of
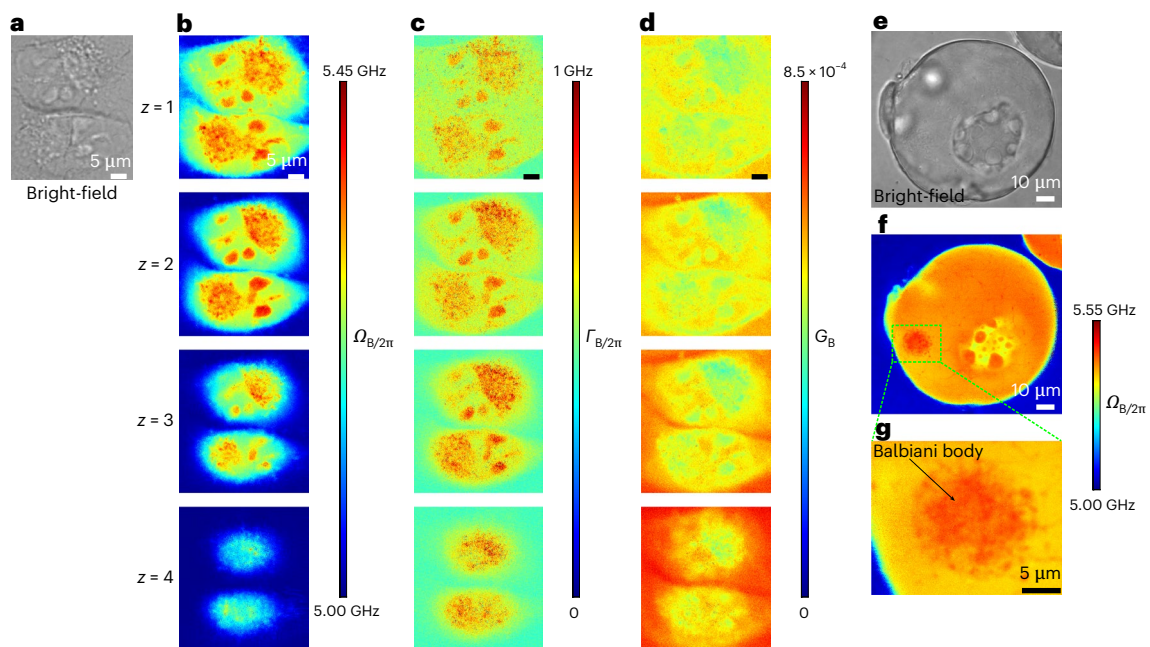
Fig. 3 | PL-SBS imaging of cultured cells and zebrafish follicles. a, Bright-field image of two HeLa cells. **b–d**, Three-dimensional Brillouin imaging of two HeLa cells, showing Brillouin shift (**b**), Brillouin linewidth (**c**) and Brillouin peak gain (**d**) under 25-mW pump power and 5-mW probe power with a z step of 1 μm. The pixel time and pixel steps in **b–d** are 200 μs and 0.02 × 0.2 μm², respectively. Scale bars, 5 μm. **e**, Bright-field image of a zebrafish ovarian follicle. **f**, Brillouin

shift image of the follicle acquired with 8 mW of pump power and 4 mW of probe power, with a pixel time of 1 ms and pixel steps of 0.1 × 0.1 μm². **g**, Brillouin shift image of the zoomed-in area (green dashed box) in **f**, highlighting the Balbiani body, with a pixel time of 1 ms and pixel steps of 0.05 × 0.05 μm. Scale bars, 10 μm (**e** and **f**); 5 μm (**g**).

the pump and probe intensities. Using a pulsed illumination approach, the signal is enhanced by a factor of T/τ, where τ is the pulse width and T is the pulse period, compared with CW schemes (Methods). Although QCW-SBS has increased the Brillouin gain by a factor of ten over CW-SBS microscopy, its pulse generation approach, which amplifies a CW laser at 780 nm and subsequently chops it into pulses via an optical modulator, remains inefficient, with most of the pulse energy wasted[31]. Consequently, the peak power is limited by either the amplification capability of the CW laser or the damage threshold of the modulator, resulting in an output peak power of only 1–2 W generally[31].

To address the demand of high-peak-power, low-duty-cycle, single-frequency laser source in SBS microscopy, we developed a pulsed laser system that generates nanosecond pulses at 1,560 nm through master oscillator power amplification (MOPA) with two-stage fibre amplification, followed by pulsed second-harmonic generation (SHG) at 780 nm (Supplementary Fig. 1). In contrast to the previous 'first amplification then chopping' method, which involves substantial energy waste and inherently limited peak power, our 'first chopping then amplification' scheme effectively concentrates the pumping energy into the low-duty-cycle nanosecond pulses, resulting in high peak power generated (Fig. 1b). We achieved a peak power of 267 W at 780 nm, with a pulse width of 6 ns and a pulse rate of 1 MHz, yielding a conversion efficiency of 59% (Supplementary Fig. 2). This peak power is 100-fold higher than that of QCW-SBS. Technical details on pulse generation, amplification and frequency doubling are provided in Supplementary Fig. 1 and Methods.

Although our pulsed laser system substantially enhances the signal strength, the remaining challenge is the considerable intensity of noise generated in the two-stage fibre amplification. We first reduced the intensity noise by 3 dB through a pulse-picking scheme that generates 500-kHz pulses from an initial 1-MHz stream, in contrast to directly generating pulses at 500 kHz (Supplementary Fig. 2h). Moreover, we developed an auto-balanced detection system (Fig. 1c and Supplementary Fig. 3) specifically designed for the detection of high-peak-power

and low-duty-cycle optical pulses at 780 nm, which is not commercially available. Our auto-balanced detector achieved a 31.3-dB noise suppression at a detection frequency of 190 kHz (Supplementary Fig. 2i).

Microscope system and characterization

The pulsed pump and probe beams are focused on the same position within the sample using two high-NA (0.7) objectives (Fig. 1c and Supplementary Fig. 3), resulting in a measured spatial resolution of 0.49 × 0.49 × 2.1 μm³ (Supplementary Fig. 4).

To assess the performance of PL-SBS microscopy, we performed measurements with double-distilled water as a test sample (Fig. 2). The Brillouin shift and linewidth precision, key indicators of Brillouin imaging quality, were evaluated as functions of the pixel dwell time (Fig. 2a). Under a pixel time of 200 μs and a total average power of 30 mW on the sample, we achieved a shift precision of 7.7 MHz and a linewidth precision of 29 MHz, with a pulse width of 6 ns and a pulse rate of 500 kHz (Fig. 2d–f). These results are comparable with those obtained using QCW-SBS microscopy, which requires a 100-fold longer pixel dwell time of 20 ms under similar optical power[31]. The measured water Brillouin linewidth of 440 MHz (Fig. 2d) corresponds to a spectral resolution of 132 MHz, accounting for the 0.7 NA broadening, lock-in amplifier broadening and pulse Fourier transform. This value is obtained by subtracting the measured Brillouin linewidth of 308 MHz for water under low-NA (0.033) objectives[29]. Note that the measured water linewidth is 40 MHz larger than the CW-SBS microscopy and 20 MHz smaller than the QCW-SBS microscopy. Figure 2b illustrates the relationship between shift and linewidth precision as functions of pump power, with the probe power held constant at 5 mW. The slope of the fit is approximately −1, suggesting that precision is inversely proportional to pump power, which is in good agreement with the theory (Methods).

We further optimized the pulse width by measuring the precision and linewidth at various pulse widths and maintaining constant average pump and probe powers (Fig. 2c). A pulse width of 6 ns was
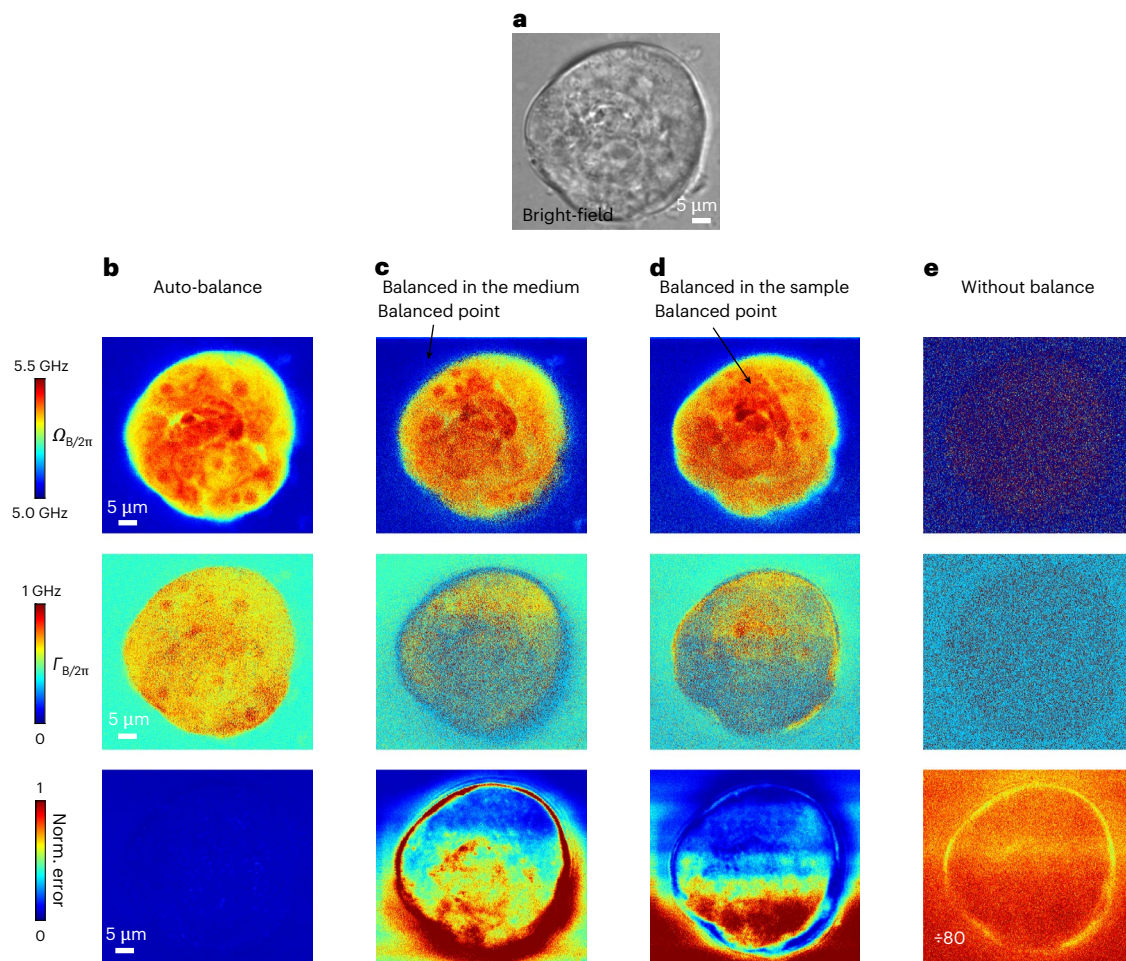
Fig. 4 | PL-SBS imaging of a patient-derived lung cancer tumour organoid.
a, Bright-field image of a patient-derived lung cancer tumour organoid.
b–**e**, Brillouin images obtained using different detection approaches: auto-balanced detection (**b**), balanced detection targeted in the medium (**c**), balanced detection targeted in the organoid (**d**) and without balance detection (**e**). For each detection approach, the top, middle and bottom panels correspond to Brillouin shift, Brillouin linewidth and peak normalized fitting error, respectively. Norm. refers to peak normalized. Average pump and probe powers are 25 mW and 5 mW, respectively, with a pixel time of 200 μs and pixel steps of 0.02×0.2 μm². Scale bars, 5 μm. In **e**, the error has been divided by a factor of 80 for clarity.

selected as optimal, offering a balance between enhanced precision and linewidth broadening, thereby achieving high spectral precision and resolution.

SBS imaging of phantom with 5-μs pixel dwell time

To further demonstrate the performance of the PL-SBS microscopy targeting specific mechanically contrasting frequency, we imaged a phantom containing oil and agarose, using Brillouin gain for contrast. Brillouin imaging was performed at frequencies of 3.91 GHz and 5.03 GHz, corresponding to Brillouin shifts of oil and agarose gel, respectively (Supplementary Fig. 5). We achieved a pixel dwell time of 5 μs, with a total average power of 30 mW, corresponding to an excitation energy of 150 nJ, which is 150 times lower than that used in CW-BGM[38].

Low-phototoxicity imaging of cells and zebrafish follicles

To demonstrate the performance of the pulsed laser system in biomechanical microscopy, we first imaged various cell lines, including HeLa cells, mouse fibroblasts (NIH/3T3), human leukaemia (MOLM-13) and human osteosarcoma (U-2 OS) cells (Fig. 3 and Supplementary Fig. 6). High-quality images of Brillouin shift, linewidth and gain across different z planes in HeLa cells are presented in Fig. 3b–d. In particular, subcellular structures such as nucleoli exhibited higher Brillouin shifts and

linewidths, yet lower Brillouin gain, compared with the nucleoplasm. Each imaging plane, containing $2,000 \times 220$ pixel², was acquired within 88 s. To assess phototoxicity, we introduced propidium iodide (PI), a dye commonly used in cell viability assays, into the cell culture. Two hours post-Brillouin imaging ($n = 10$ cells), no fluorescence signal was detected (Supplementary Fig. 6j), indicating the low phototoxicity of PL-SBS microscopy. As a control, fluorescence was evident in cells with membrane or chromosomal damage within the same dish (Supplementary Fig. 6l). Note that the PI dye assay only indicates the cell membrane integrity. To ensure there is no perturbation to the cells, future studies should measure cellular stress markers such as cell-doubling rates and mutation frequencies.

We then investigated spatial variations in Brillouin shift within the zebrafish ovarian follicle (Fig. 3e–g). This study demonstrates that the Balbiani body, a non-membrane subcellular compartment[39–41], exhibits a higher Brillouin shift, suggesting higher stiffness relative to its surrounding regions. This finding underscores the high spatial resolution and sensitivity of the PL-SBS microscope.

High-quality organoid imaging with auto-balanced detection

To assess the performance of our auto-balanced detection for biomechanical imaging, we conducted a comparative study of Brillouin images, including Brillouin shift, linewidth and fitting error (calculated
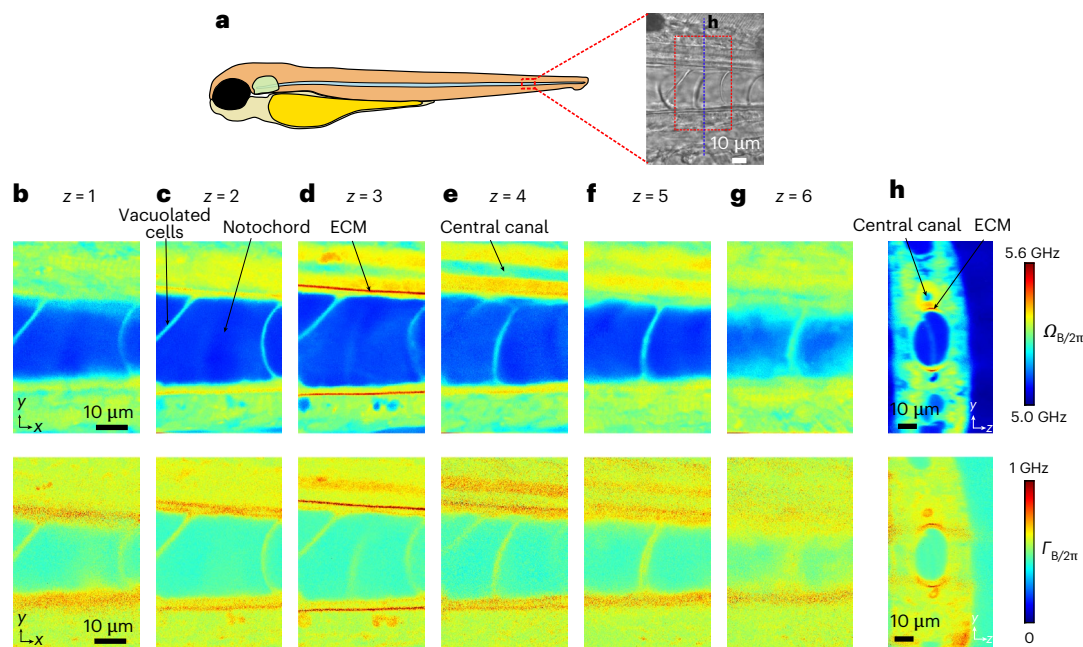
Fig. 5 | PL-SBS imaging of zebrafish larvae. a, Illustration of a zebrafish larvae, with the imaging region indicated by a dashed red box, alongside a bright-field image of the notochord region at the 3-dpf stage. **b–g,** Three-dimensional Brillouin images of the *x–y* plane at different *z*-depths within the region marked by the red box in **a**: *z* = 0 μm (**b**), 3 μm (**c**), 6 μm (**d**), 9 μm (**e**), 12 μm (**f**) and 15 μm (**g**). The top images in **b–g** represent the Brillouin shift, whereas the bottom images show the Brillouin linewidth. **h,** Cross-sectional Brillouin images of the *y–z* plane along the blue dashed line in **a**. Average pump and probe powers for all Brillouin images are 8 mW and 4 mW, respectively, with a pixel time of 2 ms and pixel steps of 0.1 × 0.2 μm². Scale bars, 10 μm.

as the root mean square difference between the measured spectrum at each pixel and the Lorentzian fit) of patient-derived lung cancer tumour organoid under four imaging conditions (Fig. 4): auto-balanced detection, balanced detection targeted in the medium, balanced detection targeted within the organoid and imaging without balanced detection. Utilizing the auto-balanced detection approach, subcellular details of cells within the organoid were clearly resolved (Fig. 4b), whereas these details were not detectable either with balanced detection (Fig. 4c,d) or without balanced detection (Fig. 4e). Overall, our auto-balanced detection method produced substantially higher image quality and minimized fitting errors compared with both types of balanced detection (targeted in the medium or within the organoid) and the unbalanced detection approach, highlighting the importance of our auto-balanced detection.

To further demonstrate the low phototoxicity of our approach, we performed organoid time-lapse imaging. In this experiment, patient-derived lung cancer organoids were imaged on days 3, 5 and 7 post-seeding (Supplementary Fig. 7). Following each imaging session, the organoids were returned to the incubator. The time-lapse images show organoid development after Brillouin imaging, providing an additional assessment of low phototoxicity.

Furthermore, we performed the continuous 2D imaging of the organoid with auto-balanced detection over a 2-h period. The quality of the Brillouin image and the fitting errors remained consistent throughout, demonstrating the long-term stability of both pulsed laser system and auto-balanced detection. These results show the use of auto-balanced detection in high-performance Brillouin microscopy and demonstrate the system's ability to resolve cellular structures within complex multicellular arrangements, which is challenging for conventional contact or bead-based methods[19]. These findings suggest that our pulsed laser system, in conjunction with the auto-balanced detection, holds promise for advancing the SBS microscopy in medical research[42,43], particularly in studying complex biological samples such as organoids.

High-specificity PL-SBS imaging in zebrafish larvae

Next, to validate the high spectral resolution of the PL-SBS microscope and its capability to distinguish different components within a heterogeneous biological sample, we imaged the notochord region of a live zebrafish larvae at 3 days post-fertilization (3 dpf) (Fig. 5). High-quality lateral (Fig. 5b–g) and axial (Fig. 5h) Brillouin images with both shift and linewidth contrasts were acquired, clearly revealing the vacuolated cells, central canal and extracellular matrix (ECM). Representative Brillouin spectra, ranging from 4.25 GHz to 6.5 GHz, for the central canal and ECM regions are presented in Supplementary Fig. 8a,b. The spectra exhibit asymmetric shapes, indicative of the presence of multiple constituents. Using double-peak Lorentzian fitting, we identified Brillouin shifts of 5.03 GHz (cerebrospinal fluid) and 5.34 GHz (beating cilia) within the central canal of the spinal cord, as well as shifts of 5.32 GHz (surrounding tissue) and 5.59 GHz (ECM) in the ECM region. These results are consistent with those from previous QCW-SBS studies[31]. Importantly, the excitation energy used in our study was 45 times lower than in previous work[31], underscoring the efficiency and high spectral resolution of the SBS microscope based on the pulsed laser system.

Time-lapse images of *C. elegans* embryo development in vivo

As a final demonstration of the high temporal resolution facilitated by the pulsed laser system, we captured the early *C. elegans* embryo development in vivo, from the two-cell stage to the four-cell stage[44] (Fig. 6 and Supplementary Video 1). We acquired 2D Brillouin time-lapse images with a resolution of 467 × 120 pixel² over 56 s, with a 1.5-min interval between the frames (Fig. 6b–i). In comparison, the previous QCW-SBS microscope required more than 18 min to acquire a single 2D image at the same resolution[31,32], making it inadequate for observing the rapid dynamics of early embryo development. In our study, the nuclei exhibited lower Brillouin shifts (Fig. 6), suggesting reduced stiffness compared with the cytoplasm. This difference probably results from the cytoplasm's dense network of cytoskeletal elements, such as actin filaments and microtubules, which provide structural integrity
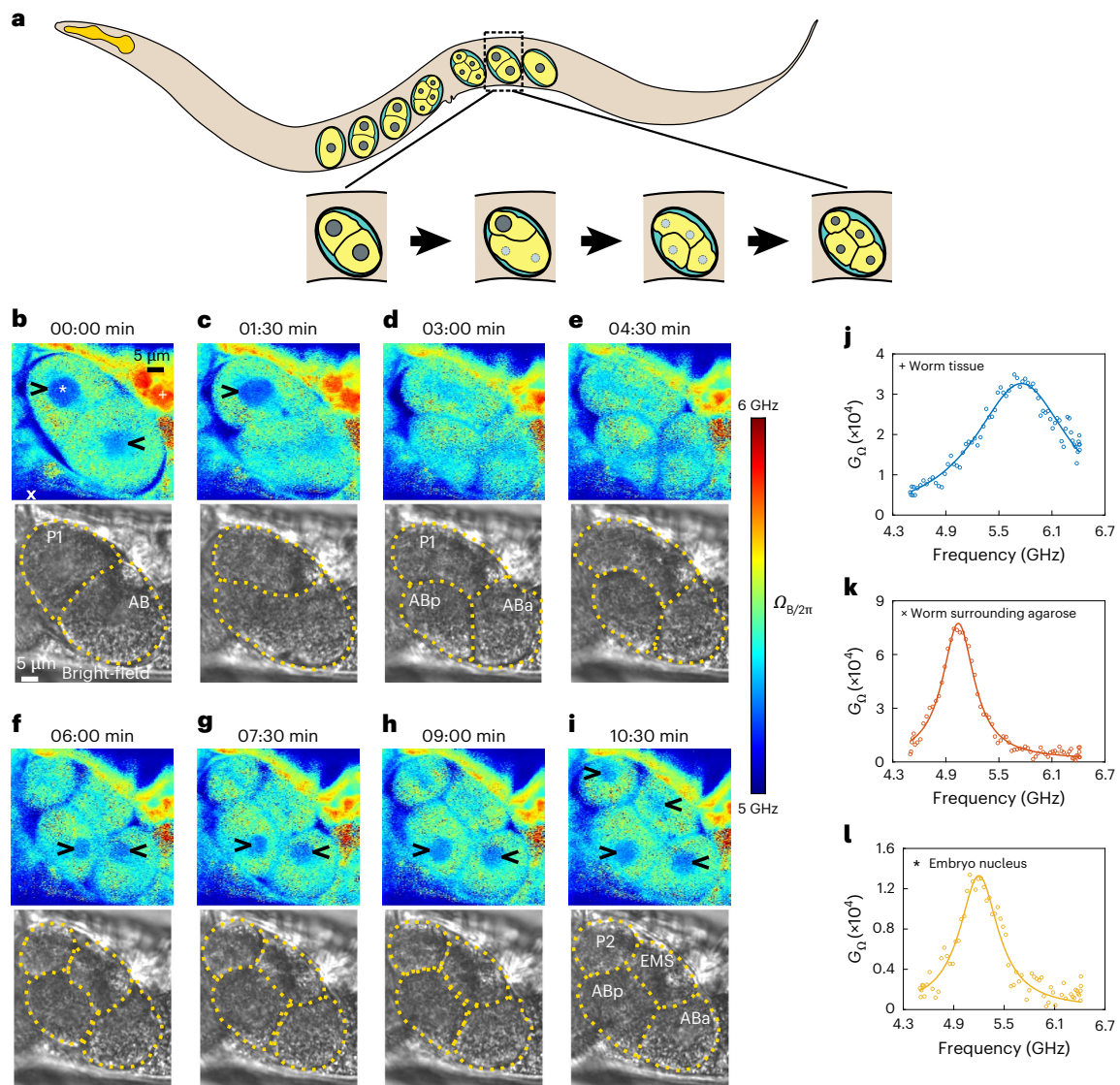
Fig. 6 | Time-lapse PL-SBS imaging of *C. elegans* embryo development in vivo.
a, Schematics of a young adult *C. elegans* and embryo development within the worm from the two-cell stage to the four-cell stage, with the embryo marked by a dashed black box. **b**–**i**, Time-lapse Brillouin shift (top) and bright-field (bottom) images of *C. elegans* embryo development from the two-cell to four-cell stage. Images were acquired at the following time points: 0 min (**b**), 1.5 min (**c**), 3.0 min (**d**), 4.5 min (**e**), 6.0 min (**f**), 7.5 min (**g**), 9.0 min (**h**) and 10.5 min (**i**). Each Brillouin image acquisition takes 56 s with a 1.5-min interval between frames. The yellow dashed lines in the bright-field images delineate the cell edges within the embryo. The black arrowheads in the Brillouin shift images point to the nuclei. The AB cell,

slightly larger, divides first into ABp and ABa cells, followed by the division of the P1 cell into P2 and EMS cells. **j**, Representative Brillouin spectrum, including the raw data and the fitting curve, in the high-shift region indicative of worm tissue (marked by a plus sign in **b**). **k**, Representative Brillouin spectrum, including the raw data and the fitting curve, in the low-shift region indicative of surrounding mounting agarose (marked by a cross in **b**). **l**, Representative Brillouin spectrum, including the raw data and the fitting curve, in the nucleus of the P1 cell (marked by an asterisk in **b**). Average pump and probe powers for all Brillouin images are 12 mW and 4 mW, respectively, with pixel time of 1 ms and pixel steps of $0.1 \times 0.4\ \mu m^2$. Scale bars, 5 μm.

and resistance to deformation. By contrast, the nucleoplasm is more fluidic, resulting in a softer environment. Note that the nucleolus in *C. elegans* embryos is much smaller than in HeLa cells, making it too small to be detected using the Brillouin microscope. Our PL-SBS microscopy system enabled rapid SBS imaging with full spectral information, as demonstrated by the spectra in Fig. 6j–l.

Remarkably, the Brillouin images also revealed nuclear dynamics associated with cell division. For instance, the nucleus in the AB cell disappeared just before division (Fig. 6b) and reappeared afterwards (Fig. 6f–i). The smaller P1 cell divided shortly after the AB cell (Fig. 6), further underscoring the advanced temporal resolution of our technique.

The peak gain observed in the embryo nuclei (Fig. 6l) was six times lower than that in the surrounding agarose (Fig. 6k), emphasizing the

challenges of achieving high temporal resolution in these measurements. Furthermore, unlike previous studies that measured *C. elegans* embryos outside of the worm by manually extracting the embryo[38] or waiting for natural egg laying[31], we conducted the embryo measurements in the worm. This approach presents additional challenges, particularly due to aberrations caused by the surrounding worm tissue, which can reduce the overlap of the pump and probe beams and, hence, requires higher system sensitivity.

Discussion

In summary, we demonstrated a reduction of approximately two orders of magnitude in both full spectrum acquisition time and laser energy at a single pixel, compared with previous SBS microscopy techniques, without notably compromising resolution,

precision or specificity (Supplementary Fig. 9). We developed a high-peak-power, low-duty-cycle pulsed laser system in conjunction with a noise-suppressing auto-balanced detection system for stimulated Brillouin microscopy. We validated the high sensitivity and spatial resolution of the pulsed-laser-based microscope by imaging cells and zebrafish follicles and revealed high-quality, subcellular details such as the Balbiani body and nucleoli. The imaging of organoids further demonstrated the effectiveness of our auto-balanced noise cancellation technique and long-term stability (>2 h) of our system. The high spectral resolution was evident from the distinct double peaks in the spectra of the central canal and ECM of zebrafish larvae. Finally, we demonstrated the speed improvements in the pulsed laser system by capturing, in vivo, the rapid biomechanical dynamics of cell division during *C. elegans* embryo development in a living worm.

Finally, quantitative comparisons of the performance of our work with the reported approaches in Brillouin microscopy are summarized in Supplementary Table 2. Recent advancements in full-field Brillouin microscopy have achieved comparable effective pixel times for biological samples and, in principle, exhibit much lower phototoxicity compared with our point-scanning PL-SBS microscopy. Our technique can be more effective in capturing fast dynamic events when the region of interest is smaller than the full field of the camera. Moreover, the imaging quality in full-field Brillouin microscopy suffers due to the compromised spectral precision and resolution[26]. By contrast, our method offers substantially improved spectral resolution, which enhances the mechanical specificity by enabling the differentiation of various mechanical components within diffraction-limited focal volumes of heterogeneous living biosamples. Additionally, it provides more precise Brillouin spectra, offering deeper insights into material properties.

The limitations of SBS microscopy include the need for an up–down microscope configuration, which restricts the types of sample that can be analysed, as well as a sample thickness limit of approximately 100–200 μm. Additionally, the Brillouin gain decreases in heterogeneous samples due to the requirement for overlap between the pump and probe beams, as demonstrated by the axial Brillouin gain image of zebrafish larvae (Supplementary Fig. 11g). To quantitatively assess the complex longitudinal modulus, our PL-SBS microscopy can be combined with techniques that measure the refractive index, such as optical diffraction tomography[22]. Furthermore, integrating Brillouin microscopy with other established mechanical probing methods is crucial for a comprehensive interpretation of the Brillouin signatures[45,46].

Further improvements in both laser noise reduction and sample scanning mechanism (Supplementary Note 3) may enable a pixel time down to 10 μs without compromising image quality, thereby making the throughput of Brillouin microscopy comparable with that of confocal fluorescence microscopy. This enhancement could promote the Brillouin imaging technique in broader applications and more challenging biomechanical research, such as transient cellular response and highly dynamic motility.

Online content

Any methods, additional references, Nature Portfolio reporting summaries, source data, extended data, supplementary information, acknowledgements, peer review information; details of author contributions and competing interests; and statements of data and code availability are available at https://doi.org/10.1038/s41566-025-01697-y.

References

1. Chaudhuri, O. et al. Effects of extracellular matrix viscoelasticity on cellular behaviour. *Nature* **584**, 535–546 (2020).
2. Fan, W. et al. Matrix viscoelasticity promotes liver cancer progression in the pre-cirrhotic liver. *Nature* **626**, 635–642 (2024).
3. Engler, A. J., Sen, S., Sweeney, H. L. & Discher, D. E. Matrix elasticity directs stem cell lineage specification. *Cell* **126**, 677–689 (2006).
4. Franz, C. M. & Puech, P. H. Atomic force microscopy: a versatile tool for studying cell morphology, adhesion and mechanics. *Cel. Mol. Bioeng.* **1**, 289–300 (2008).
5. Kennedy, B. F., Wijesinghe, P. & Sampson, D. D. The emergence of optical elastography in biomedicine. *Nat. Photon.* **11**, 215–221 (2017).
6. Scarcelli, G. & Yun, S. Confocal Brillouin microscopy for three-dimensional mechanical imaging. *Nat. Photon.* **2**, 39–43 (2008).
7. Koski, K. J. et al. Non-invasive determination of the complete elastic moduli of spider silks. *Nat. Mater.* **12**, 262–267 (2013).
8. Scarcelli, G. et al. Noncontact three-dimensional mapping of intracellular hydromechanical properties by Brillouin microscopy. *Nat. Methods* **12**, 1132–1134 (2015).
9. Elsayad, K. et al. Mapping the subcellular mechanical properties of live cells in tissues with fluorescence emission—Brillouin imaging. *Sci. Signal.* **9**, rs5 (2016).
10. Mattana, S. et al. Non-contact mechanical and chemical analysis of single living cells by microspectroscopic techniques. *Light: Sci. Appl.* **7**, 17139 (2018).
11. Antonacci, G. et al. Background-deflection Brillouin microscopy reveals altered biomechanics of intracellular stress granules by ALS protein FUS. *Commun. Biol.* **1**, 139 (2018).
12. Prevedel, R. et al. Brillouin microscopy: an emerging tool for mechanobiology. *Nat. Methods* **16**, 969–977 (2019).
13. Palombo, F. & Fioretto, D. Brillouin light scattering: applications in biomedical sciences. *Chem. Rev.* **119**, 7833–7847 (2019).
14. Margueritat, J. et al. High-frequency mechanical properties of tumors measured by Brillouin light scattering. *Phys. Rev. Lett.* **122**, 018101 (2019).
15. Antonacci, G. et al. Recent progress and current opinions in Brillouin microscopy for life science applications. *Biophys. Rev.* **12**, 615–624 (2020).
16. Zhang, J. & Scarcelli, G. Mapping mechanical properties of biological materials via an add-on Brillouin module to confocal microscopes. *Nat. Protoc.* **16**, 1251–1275 (2021).
17. Poon, C. et al. Brillouin imaging for studies of micromechanics in biology and biomedicine: from current state-of-the-art to future clinical translation. *J. Phys. Photonics* **3**, 012002 (2021).
18. Keshmiri, H. et al. Brillouin light scattering anisotropy microscopy for imaging the viscoelastic anisotropy in living cells. *Nat. Photon.* **18**, 276–285 (2024).
19. Kabakova, I. et al. Brillouin microscopy. *Nat. Rev. Methods Primers* **4**, 8 (2024).
20. Schlüßler, R. et al. Mechanical mapping of spinal cord growth and repair in living zebrafish larvae by Brillouin imaging. *Biophys. J.* **115**, 911–923 (2018).
21. Bevilacqua, C. et al. Imaging mechanical properties of sub-micron ECM in live zebrafish using Brillouin microscopy. *Biomed. Opt. Express* **10**, 1420–1431 (2019).
22. Schlüßler, R. et al. Correlative all-optical quantification of mass density and mechanics of subcellular compartments with fluorescence specificity. *eLife* **11**, e68490 (2022).
23. Zhang, H. et al. Motion-tracking Brillouin microscopy for in-vivo corneal biomechanics mapping. *Biomed. Opt. Express* **13**, 6196–6210 (2022).
24. Bevilacqua, C. et al. High-resolution line-scan Brillouin microscopy for live imaging of mechanical properties during embryo development. *Nat. Methods* **20**, 755–760 (2023).
25. Zhang, J. et al. Rapid biomechanical imaging at low irradiation level via dual line-scanning Brillouin microscopy. *Nat. Methods* **20**, 677–681 (2023).
26. Bevilacqua, C. & Prevedel, R. Full-field Brillouin microscopy based on an imaging Fourier-transform spectrometer. *Nat. Photon.* https://doi.org/10.1038/s41566-025-01619-y (2025).

27. Remer, I. & Bilenca, A. Background-free Brillouin spectroscopy in scattering media at 780 nm via stimulated Brillouin scattering. *Opt. Lett.* **41**, 926–929 (2016).

28. Remer, I. & Bilenca, A. High-speed stimulated Brillouin scattering spectroscopy at 780 nm. *APL Photon.* **1**, 061301 (2016).

29. Remer, I. et al. High-sensitivity and high-specificity biomechanical imaging by stimulated Brillouin scattering microscopy. *Nat. Methods* **17**, 913–916 (2020).

30. Rosvold, J. R. et al. Stimulated Brillouin scattering flow cytometry. *Biomed. Opt. Express* **15**, 6024–6035 (2024).

31. Yang, F. et al. Pulsed stimulated Brillouin microscopy enables high-sensitivity mechanical imaging of live and fragile biological specimens. *Nat. Methods* **20**, 1971–1979 (2023).

32. Chow, D. M. & Yun, S.-H. Pulsed stimulated Brillouin microscopy. *Opt. Express* **31**, 19818–19827 (2023).

33. Bilenca, A. et al. Current state of stimulated Brillouin scattering microscopy for the life sciences. *J. Phys. Photonics* **6**, 032001 (2024).

34. Shaashoua, R. et al. Enhancing mechanical stimulated Brillouin scattering imaging with physics-driven model selection. *Laser Photon. Rev.* **18**, 2301054 (2024).

35. Dingjan, J. et al. A frequency-doubled laser system producing ns pulses for rubidium manipulation. *Appl. Phys. B* **82**, 47–51 (2006).

36. Freudiger, C. et al. Stimulated Raman scattering microscopy with a robust fibre laser source. *Nat. Photon.* **8**, 153–159 (2014).

37. Crisafi, F. et al. In-line balanced detection stimulated Raman scattering microscopy. *Sci. Rep.* **7**, 10745 (2017).

38. Shaashoua, R. et al. Brillouin gain microscopy. *Nat. Photon.* **18**, 836–841 (2024).

39. Pepling, M. E., Wilhelm, J. E., O'Hara, A. L., Gephardt, G. W. & Spradling, A. C. Mouse oocytes within germ cell cysts and primordial follicles contain a Balbiani body. *Proc. Natl Acad. Sci. USA* **104**, 187–192 (2007).

40. Boke, E. et al. Amyloid-like self-assembly of a cellular compartment. *Cell* **166**, 637–650 (2016).

41. Lei, L. & Spradling, A. C. Mouse oocytes differentiate through organelle enrichment from sister cyst germ cells. *Science* **352**, 95–99 (2016).

42. Boj, S. F. et al. Organoid models of human and mouse ductal pancreatic cancer. *Cell* **160**, 324–338 (2015).

43. Clevers, H. Modeling development and disease with organoids. *Cell* **165**, 1586–1597 (2016).

44. Shelton, C. A. & Bowerman, B. Time-dependent responses to *glp-1*-mediated inductions in early *C. elegans* embryos. *Development* **122**, 2043–2050 (1996).

45. Nikolić, M., Scarcelli, G. & Tanner, K. Multimodal microscale mechanical mapping of cancer cells in complex microenvironments. *Biophys. J.* **121**, 3586–3599 (2022).

46. Handler, C., Testi, C. & Scarcelli, G. Advantages of integrating Brillouin microscopy in multimodal mechanical mapping of cells and tissues. *Curr. Opin. Cell Biol.* **88**, 102341 (2024).

Methods

Principle of a PL-SBS microscope

The SBS microscope is based on the SBS between two focused counterpropagating laser beams, that is, pump (ω_1) and probe (ω_2) beams, mediated by the excited acoustic phonons at the focal spot in the sample. When the differential frequency $\omega_1 - \omega_2$ matches the characteristic acoustic resonance at Ω_B, the pump energy is transferred to the probe beam, with the energy-transferring rate manifested as the power increment in the probe beam $\Delta P_2 = G(\Omega)P_2$, where $G(\Omega)$ is the SBG. For perfectly overlapped beams, the SBG spectrum is expressed as $G(\Omega) = g(\Omega)lP_1A^{-1}$, where $g(\Omega)$ is the Brillouin gain factor of the Lorentzian line shape centring at Ω_B with full-width at half-maximum linewidth of Γ_B, l is the interaction length between the two counterpropagating beams within the sample volume, P_1 is the pump power and A is the waist area at the focal spot. The Brillouin shift and linewidth are related with the complex longitudinal modulus of the material as $M = M' + M'' = \frac{\rho}{n^2}\frac{\pi^2 c_0^2}{\omega_1^2}\Omega_B^2(1 + i\frac{\Gamma_B}{\Omega_B})$, where M' and M'' are the storage and loss moduli accounting for the elastic and viscous properties of the sample, respectively; ρ, n and c_0 are the mass density, refractive index and speed of light in a vacuum, respectively.

The signal amplitude S in SBS imaging is determined by the time-averaged incremental power in the probe beam given by $\langle \Delta P_2 \rangle = T^{-1} \int_0^T \Delta P_2 dt$, with T being the sampling time; hence, we have $S \propto T^{-1} \int_0^T P_1 P_2 dt$. For pulsed pump and probe beams with a duty cycle of κ and fixed mean power of $\bar{P}_1$ and $\bar{P}_2$, respectively, the signal amplitude is then expressed as $S \propto T^{-1} \int_0^{\kappa T} \frac{\bar{P}_1 \bar{P}_2}{\kappa^2} dt = \kappa^{-1}\bar{P}_1\bar{P}_2$, from which it is apparent that by reducing the duty cycle of the pulsed laser, the SBG signal can be inverse proportionally improved with an enhancement factor of κ^{-1}.

Pulsed laser system

The dual-wavelength pulsed laser system for the generation of single-frequency pulsed pump and probe beams is based on MOPA for 1,560-nm optical pulses and subsequent SHG (Supplementary Fig. 1). The pump and probe beams have generally the same configuration in MOPA and SHG subsystems; hence, we just take the pump beam as an illustration here.

The MOPA unit is constructed with polarization-maintaining fibre-optic components. It is designed to amplify the single-frequency seed with nanosecond pulse width from milliwatts to hundreds of watts. To achieve a gain up to 50 dB and suppressing the amplified spontaneous emission (ASE) noise, a two-stage amplification scheme is used, with each stage providing a maximum gain of over 25 dB. The CW single-frequency seed at 1,560.48 nm is an external cavity diode laser with a power of 15 mW and linewidth of 10 kHz. The CW pump seed is first split into two beams by a 50:50 fibre coupler, with one beam beating with the probe seed for the heterodyne detection of the differential frequency by a fast photodetector (1544-B, Newport) and a frequency counter (53230A, Keysight) to get the exact frequency shift of the SBS. The other beam of the pump seed is chopped into pulses by a semiconductor optical amplifier (SOA; IPSAD1514-6210, Inphenix) mounted on a pulsed SOA driver. The seed pulse has an extinction ratio of approximately 50 dB. Optical pulses with an adjustable pulse width from 2 to 12 ns are generated by the SOA with both repetition rate f_r and phase of the pulses determined by the external triggering signal from an electrical pulse generator (DG922 Pro, Rigol). After passing the optical isolator, the pulsed seed is first preamplified by a piece of erbium-doped fibre (PM-ESF-7/125, Coherent) with a length of 2.5 m and backward pumped by a single-mode 976-nm laser diode (976LD-1-0-0, Aerodiode). A band-pass filter centred at 1,560.6 nm with a spectral bandwidth of 0.5 nm is used to filter out the ASE noise. Then, the pulsed laser is boost-amplified by a Yb/Er co-doped double-cladding fibre (PM-EYDF-10/125-XPH, Coherent), which is backward pumped[47]

at 940 nm. The 940-nm pump is from two identical multimode laser diodes (940LD-2-0-0, Aerodiode), with each offering a pumping power up to 10 W and coupled into the cladding of the gain fibre through a 2 + 1 × 1 combiner (PMPSC-21-F-15, DK Photonics). The remaining of the backward pump beam is filtered out by a cladding power stripper spliced before the double-cladding gain fibre. For the typical pulse rate of 1 MHz and width of 6 ns, we achieved an average 1,560-nm output of 3.3 W at a pumping power of 13.6 W, corresponding to a peak power of 560 W for the 1,560-nm pulse. The slope and mean optical-to-optical efficiencies for the boost-amplifying stage are 25% and 24%, respectively (Supplementary Fig. 2a). After the combiner, another cladding power stripper is spliced to remove both back-scattered 940-nm pump and ASE noise. An optical isolator is spliced to cut-off any possible back-reflection into the MOPA unit. Before collimating out the 1,560-nm pulsed laser, a section of the coreless fibre is spliced with an angled terminal, which works as an end cap to moderately expand the beam size and hence avoid surface damage. An aspheric lens (#29-988, Edmund) is used to collimate the 1,560-nm pulses generated in the MOPA unit. To suppress the nonlinear effects in the silica fibre during the two-stage amplification, such as SBS and modulation instability, which limit the output power and increase the pulse train noise, the length of the fibre components are kept as short as possible. Compared with the additional seed laser for the probe beam as implemented here, the probe seed may alternatively be frequency shifted from the pump seed using an electro-optic modulator driven by a frequency-tunable microwave source, in which scheme the frequency counter may then be unnecessary.

The 1,560-nm pulsed laser is then frequency doubled in the SHG unit by using a periodically poled lithium niobate crystal. A dichroic mirror (DMLP1180, Thorlabs) is used first to filter out the core-guided 940-nm pump and Yb ASE light. We use a half-wave plate and a polarization beamsplitter (PBS) for power control as well as s-polarization filtering to comply with the quasi-phase-matching condition of the periodically poled lithium niobate[48]. A plano-convex lens is used to couple the 1,560-nm beam into the periodically poled lithium niobate crystal (40-mm long for 1,560 nm, Covesion). The crystal is mounted in an oven with a stabilized temperature of around 90 °C, at which optimal quasi-phase matching is achieved. Both fundamental and frequency-doubled beams are collimated by another lens and then separated from each other with a dichroic mirror. The diameter of the output 780-nm beam is measured to be ~1.2 mm. For the typical 1-MHz pulse rate and 6-ns pulse width, we achieved a maximum average power of 1.6 W from the SHG unit, corresponding to a peak power of 267 W with a conversion efficiency of 59% (Supplementary Fig. 2b). For the pulsed pump beam, a volume Bragg grating (SPC-780, OptiGrate) with a spectral bandwidth less than 50 pm is used to filter out the frequency-doubled ASE noise centring at 780 nm. Both power and polarization stability of our pulsed laser system are measured at the 780-nm output. For the 1-MHz rate, 6-ns width and 0.73-W average output power, the peak-to-peak and r.m.s. power fluctuations are measured to be 9.1% and 1.5%, respectively, over a 5-h monitoring. Polarization extinction ratio over 24 dB is also achieved (Supplementary Fig. 2d). Frequency stability of the laser system is demonstrated by monitoring the beating frequency between the pump and probe seed lasers over 1 h, which shows a peak-to-peak and r.m.s. differential frequency fluctuation within 0.93 MHz and 0.13 MHz, respectively, at 780 nm (Supplementary Fig. 2e). The output spectra of the seed laser, first- and second-stage fibre amplification and the SHG are measured by an optical spectrum analyser (AQ6374, Yokogawa; Supplementary Fig. 2f,g). The ASE floor is measured to be about 65 dB below the main output at 780 nm.

Pulse picking by acousto-optic modulators (AOMs; AOMO 3200-124, G&H) is adopted to reduce the intensity noise for both pump and probe beams. A pulse train with a lower repetition rate tends to generate higher ASE, due to longer time span under continuous pumping

without a seed signal to be amplified. Compared with the direct generation of pulses of 500-kHz repetition rate or lower, the scheme of the first generation of 1-MHz repetition rate and subsequently picking one pulse out of every two pulses or more, that is, pulse rate down to 500 kHz or lower, results in reduced intensity noise ranging from 3 dB to 1 dB for pulse width ranging from 11 ns to 2 ns (Supplementary Fig. 2h). The 200-ns electrical picking pulses driving the AOM are synchronized with the triggering pulses for SOAs. Aspheric lens pair (#18-080, Edmund) is used to couple the beams into and out of the AOM. For the pump beam, its AOM also performs intensity modulation, with the modulation frequency f_m determined by a lock-in amplifier (LIA; MFLI-5MHz, Zurich Instruments). Both pump and probe beams are coupled into a PM780 optical fibre using an aspheric lens (PAF2A-5B, Thorlabs). The pump beam is then directly sent to the microscope, whereas the probe beam is first divided into two beams by a 50:50 fibre coupler, with one beam to interact with the pump light in the microscope and the other beam serving as the reference for auto-balanced detection.

PL-SBS microscope and detection system

The detailed setup of the PL-SBS microscope and auto-balanced detection is shown in Supplementary Fig. 3. For the microscope, both pump and probe beams are collimated using an aspheric lens (#49-115, Edmund) with an output beam diameter of 5.9 mm. A quarter-wave plate is used to convert the linearly polarized probe beam into a right circularly polarized beam. L1 lens pair (#49-356, Edmund) is immaterial to both pump and probe beams, but necessary for realizing Kohler illumination in bright-field imaging, in which the surface of the Ø1-mm multimode fibre coupling a light-emitting diode (M530L4, Thorlabs) is conjugated to the back-focal plane of the upper objective (Objective 1) for uniform illumination on the sample. The pump beam is p polarized by the half-wave plate and transmits through the PBS subsequently. Quarter-wave plate 2 then transforms the pump beam into a left circularly polarized beam. The opposite circularly polarized probe and pump beams are focused into the same spot in the sample by the two opposed objectives (LUCPLFLN60X, Olympus) with an NA of 0.7. The back apertures of both the objectives are overfilled by the Ø5.9-mm laser beams for full utilization of the NA. In PL-SBS imaging, the focal point is fixed, whereas the sample is zigzag scanned by a three-axis piezo stage (L3S-D10300-XYZ300, nanoFaktur). After experiencing the SBG during the phonon-mediated interaction with the pump beam, the probe beam is re-collimated by the lower objective (Objective 2), then turns into s polarization after quarter-wave plate 2 and is finally reflected by the PBS for subsequent detection and demodulation. When flip mirrors FM1 and FM2 are flipped down, bright-field imaging is activated, where the sample is imaged onto camera C1 (BFLY-U3-23S6M-C, FLIR) by tube lens L2 (TTL165-A, Thorlabs) with a focal length of 165 mm. To perform wide-field fluorescence imaging targeting PI, excitation (MF525-39, Thorlabs) and emission (MF620-52, Thorlabs) filters are inserted after the light-emitting diode and before the camera, respectively.

The auto-balanced detection unit is to suppress the common-mode intensity noise within the pulsed probe beam. It has one port (that is, signal port) from the output of the PL-SBS microscope and the other port (that is, reference port) directly from one beam of fibre-coupler-split probe source. The amplified probe beam from the signal port triple passes the custom-made rubidium-85 gas cell (Ø25 × 150 mm), which is heated to a temperature of 95 °C, to filter out the back-scattered and/or reflected pump beam. The optical signal is detected by reverse-biased photodiodes (FDS1010, Thorlabs) with the photoelectric current separated into d.c. and radio-frequency parts by the bias-tee (ZFBT-4R2GW+, Mini-Circuits). The d.c. parts of the signal and reference are sent to the two differential ports of the proportional–integral–derivative controller (LB1005-S, Newport), the output of which is to drive the 780HP fibre pigtailed electronic variable optical attenuator (V800, Thorlabs), so that the optical power

in the reference beam is kept at the same level of the signal beam, even if the signal beam experiences substantial power change due to non-uniform transparency in the scanned sample. The radio-frequency components are first low-pass filtered to cut-off the carriers at f_r as well as its high harmonics, with only the first-order signal at f_m passing through the low-pass filters and entering the LIA. The LIA works in the differential-input mode, so that the common-mode intensity noise in the probe beam is substantially suppressed, providing a matched optical path for the signal and reference beam. For PL-SBS imaging with a 200-µs pixel time and a 500-kHz pulse repetition rate, the noise equivalent power (NEP) bandwidth of the LIA is set to 40 kHz, and the optimal modulation frequency is determined to be 190 kHz, where the auto-balanced detection achieves intensity noise reduction as large as 31.3 dB (Supplementary Fig. 2i). In SBS imaging, the frequency of the probe beam is sawtooth scanned, generally spanning 2 GHz and completed within the pixel time. The demodulated SBG signal from the LIA, along with the d.c. level of the probe beam, which is proportional to the mean probe power on the photodetector, and the instantaneous voltage driving the frequency scanning are collected by a data acquisition card (USB-6343, National Instruments) for construction of the SBG spectra.

Hardware control, including the piezo stage moving, frequency scanning, data acquisition and interdevice synchronization, is executed by a custom-built LabVIEW 2022 Q3 program. The spectral data processing is based on a custom program implemented in Python 3.9 with the details given in Supplementary Note 2.

Performance characterization and imaging acquisition

Measurement of spatial resolution. The spatial resolution characterization of the PL-SBS microscope includes determination of both lateral (that is, x and y) and axial (that is, z) resolutions. The lateral resolution is quantified by the SBS imaging of polydimethylsiloxane (PDMS) bead in 1% (w/v) agarose with the focal spot on the same plane as the bead centre (Supplementary Fig. 4a). The Brillouin shift of the agarose gel and PDMS are measured to be 5.03 GHz and 4.2 GHz, respectively (Supplementary Fig. 4c). By fitting the measured spectra at a fixed Brillouin shift of the agarose gel, the signal amplitude has its distribution shown in Supplementary Fig. 4b. Then, the signal amplitudes of agarose gel across the bead boundary are fitted with an error function along both x and y axes, giving a lateral spatial resolution of 0.49 µm (Supplementary Fig. 4d,e,i). The axial resolution is quantified by SBS imaging of the interface between double-distilled water and coverslip (Supplementary Fig. 4f). The Brillouin shift of double-distilled water is at 4.98 GHz as experimentally measured whereas that of the borosilicate coverslip is over 10 GHz higher and far away from the frequency-scanning range we set. As shown in Supplementary Fig. 4g, the SBS amplitude of water when the focal spot is scanned in the x–z plane cross through the water–glass boundary. By fitting the signal amplitude in the z direction with an error function, the axial resolution is measured to be 2.1 µm (Supplementary Fig. 4h,i). A high spatial resolution is on condition of matched overlap between the pump and probe at the same focal spot in the sample, the optimization of which is described in Supplementary Note 1.

Determination of spectral precision and spectral resolution. The characterization of spectral precision and spectral resolution are based on the SBS measurement of double-distilled water at room temperature with objectives of 0.7 NA. The SBS spectral precision includes the shift and linewidth precisions, which are quantified as the standard deviation of the Brillouin shift and linewidth, respectively, extracted from the Lorentzian fitting of $n = 300$ consecutively acquired SBS spectra with frequency ranging from 4 GHz to 6 GHz.

The spectral precision with different integration times (that is, pixel time) is measured with a pulse rate of 500 kHz and a pulse width of 6 ns (Fig. 2a). The total average power on the sample is 30 mW,

with pump and probe powers of 25 mW and 5 mW, respectively. The time–bandwidth product of 8 kHz ms is maintained for all the measurements, that is, the NEP bandwidth of the LIA is set to 40 kHz for 200-µs pixel time and 8 kHz for 1 ms. Note that the NEP of 40 kHz for 200-µs pixel time corresponds to a time constant of 3.1 µs of the LIA. A slope of roughly −0.5 for precision versus pixel time in both Brillouin shift and linewidth indicates the domination of white noise in our system for the pixel time we set. Shift and linewidth precision of 7.7 MHz and 29 MHz, respectively, is achieved for pixel time down to 200 µs (Fig. 2a,e,f) with a measured full-width at half-maximum linewidth of 0.44 GHz in water (Fig. 2d). A narrower pulse width typically increases the signal amplitude due to a higher enhancement factor, resulting in improved signal-to-noise ratio (Supplementary Fig. 2j) and precision (Fig. 2c). However, the reduced pulse width is associated with a larger laser linewidth, which causes the measured Brillouin spectra, as a convolution between the laser and the intrinsic Brillouin line shapes, to broaden (Fig. 2c). The deterioration in precision for pulse widths less than 3.5 ns is attributed to the increased laser noise (Supplementary Fig. 2h), exceeding the noise cancellation capability of our auto-balanced detector. Choosing a 6-ns pulse width for performance characterization as well as SBS imaging results from the higher spectral precision compared with the longer pulse width (due to the higher enhancement factor) and moderate linewidth broadening compared with the shorter ones. Precision under different pump powers is measured with a fixed probe power of 5 mW and pixel time of 200 µs. The spectral precision scales down with the pump power, as indicated by a fitting slope of approximately −1 (Fig. 2b). Compared with the 308-MHz intrinsic SBS linewidth of water[29], the measured linewidth of 440 MHz demonstrates a spectral resolution of 132 MHz for our system, which includes NA broadening.

Pulsed laser BGM. The pulsed laser BGM is performed with a phantom sample of layered oil–agarose gel (Supplementary Fig. 5a), whose Brillouin shifts are of 3.91 GHz and 5.03 GHz, respectively (Supplementary Fig. 5e). By keeping the differential frequency between the pump and probe beams at the peak of either oil or agarose gel, the Brillouin gain across the interface is mapped with a pixel time of 5 µs and an NEP bandwidth of 40 kHz (Supplementary Fig. 5b,c). The gain profiles along the axial direction are given in Supplementary Fig. 5d.

Sample preparation and imaging parameters
Chemical samples. The water sample is prepared by sandwiching 20-µl double-distilled water between two #1.5 coverslips, which are separated by two imaging spacers (Grace Bio-Labs SecureSeal) with a thickness of 240 µm. To prepare the sample of PDMS beads in agarose gel, 5 µl of 1% w/v low-melting-point agarose water solution is first dropped on the surface of a #1.5 coverslip, on which a 120-µm-thick spacer is attached beforehand. After gelation of the agarose solution, PDMS beads with a mean diameter of 10 µm are deposited on the gel surface, followed by the immediate addition of 7-µl agarose solution. Then, the sample is sealed by covering another #1.5 coverslip. The oil–agarose gel sample is made by first dropping 5-µl low-melting-point agarose solution on the surface of a #1.5 coverslip adhered with a 120-µm-thick spacer. Refractive-index oil (Cargille Labs, n_D of 1.414) of 5 µl is then added on top of the agarose gel and the sample is finally sealed with another #1.5 coverslip.

Cells (including viability test parameter). Cell lines were purchased from Cobioer and were maintained according to the guidance from American Type Culture Collection. U-2 OS (CBP60238), human cervical carcinoma cell line HeLa (CBP60232) and mouse fibroblasts NIH/3T3 (CBP60317) were cultured in Dulbecco's modified Eagle's medium (Gibco, 11960044) supplemented with 10% (v/v) foetal bovine serum (Gibco, 30044333) and 100 U ml⁻¹ penicillin–streptomycin (Gibco, 15140122). Cells were seeded on polyacrylamide-gel-coated dishes

(Matrigen, SV3510-EC-12) at a density of 5,000 cells cm⁻² and allowed to adhere overnight before imaging.

MOLM-13 (CBP60678) was cultured in RPMI-1640 (Gibco, 1049101) supplemented with 10% (v/v) foetal bovine serum and 100 U ml⁻¹ penicillin–streptomycin. Dishes (MatTek, P35G-1.5-14-C) were coated with 0.1 mg ml⁻¹ poly-D-lysine (Gibco, A3890401) for 1 h at 37 °C before seeding the cells at a density of 5,000 cells cm⁻². The cells were allowed to adhere for 1 h at 37 °C before imaging. Cells have been authenticated by short tandem repeat analysis and mycoplasma detection.

To test the cell viability after Brillouin imaging with the PL-SBS microscope, we added PI (Sigma-Aldrich, P4170-10MG) dye in the cell dishes with a volume ratio to the cell medium of 15 µl in 1 ml.

Lung cancer organoids. Malignant pleural effusion samples were obtained from lung cancer patients by thoracentesis at Shanghai Ninth People's Hospital. The research protocol was approved by the Ethics Committee of Shanghai Ninth People's Hospital affiliated with the Shanghai Jiao Tong University. Informed consent was obtained from patients before sample collection. Malignant serous effusions were collected aseptically in heparinized sterile bottles, and centrifuged at 300g for 5 min at 4 °C. Pellets were resuspended in lung cancer organoid medium (Dulbecco's modified Eagle's medium/F12 (Gibco, 12634-010) supplemented with 1X GlutaMAX (Gibco, 35050061), 10 mM of HEPES (Gibco, 15630080), 20 ng ml⁻¹ of bFGF (Peprotech, 100-18B), 50 ng ml⁻¹ of human EGF (Peprotech, AF-100-15), 1X N2 (Gibco, 17502048), 1X B27 (Gibco, 17504044), 10 µM of Y-27632 (MCE, HY-10071), 5 mM of nicotinamide (MCE, HY-B0150), 1 mM of N-acetyl-L-cysteine (Sigma, A9165), 3 µM of SB202190 (MCE, HY-10295), 5 µM of A 83-01 (MCE, HY-10432), 10 µM of forskolin (Selleck, S2449), 3 nM of dexamethasone (Selleck, S1322) and 1% of penicillin–streptomycin (Gibco, 15140122)).

Then, 50 µl of the suspension was mixed with 100 µl of Matrigel (Corning, 356231) and seeded on prewarmed six-well culture plates (Thermo Scientific, 140675) at 37 °C for 30 min. The plates were inverted to solidify at 37 °C for 30 min followed by the addition of 3 ml of medium per well. The lung cancer organoid medium was replaced every 3–4 days.

For passaging, lung cancer organoids were harvested using cold Dulbecco's phosphate-buffered saline and incubated with TrypLE Express (Gibco, 12604021) for 10 min at 37 °C for dissociation. The dissociated organoids were resuspended in the lung cancer organoid medium with Matrigel (1:2 ratio) and reseeded on a glass-bottomed dish (MatTek, P35G-1.5-14-C).

Zebrafish. *Zebrafish ovarian follicle preparation*. Fish maintenance and embryo collection were carried out as described in ref. 49. Here 5–24-month-old females from WT AB strains were used, fish were bred in the zebrafish facility at LSI Zhejiang University according to local regulations. All procedures were approved by the Ethics Committee of Zhejiang University regulating animal care and usage.

Zebrafish ovarian follicle isolation was performed following previously described protocols[50,51]. Female zebrafish were anaesthetized in 0.02% tricaine and euthanized by decapitation. Ovaries were harvested in a culture medium consisting of 70% Leibovitz's L-15 medium with L-glutamine, pH 8.0 (Gibco), supplemented with 50 U ml⁻¹ of penicillin–streptomycin and 0.5% of bovine serum albumin (Sigma-Aldrich). Stage I follicles (60–100 µm in diameter) were isolated from the ovaries through gentle pipetting with a glass Pasteur pipette, followed by dissection using forceps under an Olympus SZX16 stereomicroscope. The isolated follicles were then mounted in 0.6% low-melting-point agarose (Sangon Biotech).

Zebrafish larva preparation. Transgenic zebrafish larvae were in the casper background. The fish was mounted at 3 dpf in the centre of a Petri dish (MatTek, P35G-1.5-14-C) with 1% (w/v) low-melting-point agarose and 0.016% (w/v) tricaine (for immobilization purpose).

A coverslip was used to cover the agarose before solidifying to allow the access of the sample by two objectives.

C. elegans. *C. elegans* adults of the wild-type N2 Bristol strain were centrifugally rinsed three times with M9 solution. M9 agarose was made by mixing low-melting-point agarose and levamisole in M9 solution. Then, 8 µl of M9 agarose was added on a coverslip, to which two imaging spacers (with a total thickness of 240 µm) were stacked together and stuck. The worms were transferred on the agarose pad using a sterilized platinum wire. Then, another 17 µl of low-melting-point M9 agarose was added in the imaging spacer, with a second coverslip placed on top. The early embryos were selected for Brillouin imaging in the far end of the worm's valve.

Data availability
The main data that support this study are available within the Article and its Supplementary Information. The additional raw and processed data are available via Zenodo at https://doi.org/10.5281/zenodo.15267405 (ref. 52).

Code availability
The Python GPU-accelerated SBS spectral analysis code is available via GitHub at https://github.com/yang-biophotonics-lab/sbs-python/.

References
47. Beier, F. et al. Robust 1550-nm single-frequency all-fiber ns-pulsed fiber amplifier for wind-turbine predictive control by wind lidar. In *Fiber Lasers X: Technology, Systems, and Applications* (ed. Hendow, S. T.) 86012S-1–86012S-7 (SPIE, 2013).
48. Krupa, K. et al. Polychromatic filament in quadratic media: spatial and spectral shaping of light in crystals. *Optica* **2**, 1058–1064 (2015).
49. Westerfield, M. *The Zebrafish Book. A Guide for the Laboratory Use of Zebrafish (Danio rerio)* 5th edn (Univ. Oregon Press, 2007).
50. Xia, P., Gütl, D., Zheden, V. & Heisenberg, C.-P. Lateral inhibition in cell specification mediated by mechanical signals modulating TAZ activity. *Cell* **176**, 1379–1392.e14 (2019).
51. Elkouby, Y. M. & Mullins, M. C. Methods for the analysis of early oogenesis in zebrafish. *Dev. Biol.* **430**, 310–324 (2017).
52. Qi, Y. & Yang, F. Data for the Fig 2 and Fig. 6 in the main manuscript as well as Fig. 2, Fig. 4, Fig 5, Fig 8 and Fig. 9 in the Supplementary Information. *Zenodo* https://doi.org/10.5281/zenodo.15267405 (2025).

Acknowledgements

Author contributions
F.Y. and Y.Q. conceived the project and designed the microscope. F.Y., W.-B.C. and Y.Q. designed the laser system. Y.Q. performed the experiment with help from S.Y., Z.-X.D., C.Z. and X.F. J.-R.Z. developed the Python code for Brillouin spectrum analysis. H.L. and T.M. provided cells and helped with the interpretation under the guidance of J.X. Y.-H.C. and Y.-F.W. provided zebrafish larvae and helped with the interpretation under the guidance of J.-L.D. Y.L. provided *C. elegans* and helped with the embryo development interpretation under the guidance of S.-Q.C. X.H. provided the zebrafish follicle and helped with the Balbiani body interpretation under the guidance of P.X. J.N., Y.Z. and L.S. provided the organoids. F.Y. and W.-B.C. led the project. F.Y. and Y.Q. wrote the paper with input from all authors.

Competing interests
F.Y. and Y.Q. are inventors on the Chinese patent (no. 2025107030082) that has been described in this study. J.N. and L.S. are employees of Shanghai Medsyin Biopharma. The other authors declare no competing interests.

Additional information
Supplementary information The online version contains supplementary material available at https://doi.org/10.1038/s41566-025-01697-y.

Correspondence and requests for materials should be addressed to Wei-Biao Chen or Fan Yang.

Peer review information *Nature Photonics* thanks Kareem Elsayad and the other, anonymous, reviewer(s) for their contribution to the peer review of this work.

Reprints and permissions information is available at www.nature.com/reprints.